TITLE:

Unveiling the role of differential growth in 3D morphogenesis: An inference method to analyze area expansion rate distribution in biological systems

AUTHOR(S):

Morikawa, Kentaro; Morita, Shinichi; Sakura, Kazuki; Maeno, Akiteru; Gotoh, Hiroki; Niimi, Teruyuki; Inoue, Yasuhiro

CITATION:

Morikawa, Kentaro ...[et al]. Unveiling the role of differential growth in 3D morphogenesis: An inference method to analyze area expansion rate distribution in biological systems. Journal of Theoretical Biology 2023, 575: 111650.

ISSUE DATE:

2023-11-07

URL:

http://hdl.handle.net/2433/286160

RIGHT:

© 2023 The Author(s). Published by Elsevier Ltd.; This is an open access article under the CC BY license.

京都大学学術情報リポジトリ
KURENAI 紅
Kyoto University Research Information Repository

京都大学 KYOTO UNIVERSITY
A Self-archived copy in
Kyoto University Research Information Repository
https://repository.kulib.kyoto-u.ac.jp
京都大学学術情報リポジトリ KURENAI 紅 Kyoto University Research Information Repository

Journal of Theoretical Biology 575 (2023) 111650

Contents lists available at ScienceDirect

Journal of Theoretical Biology

journal homepage: www.elsevier.com/locate/yjtbi

Unveiling the role of differential growth in 3D morphogenesis: An inference method to analyze area expansion rate distribution in biological systems

Kentaro Morikawa [a,*], Shinichi Morita [b,c], Kazuki Sakura [b], Akiteru Maeno [d], Hiroki Gotoh [e], Teruyuki Niimi [b,c], Yasuhiro Inoue [a,*]

[a] Department of Micro Engineering, Graduate School of Engineering, Kyoto University, Japan
[b] Division of Evolutionary Developmental Biology, National Institute for Basic Biology, Japan
[c] Basic Biology Program, Graduate Institute for Advanced Studies, The Graduate University for Advanced Studies, SOKENDAI, Japan
[d] National Institute of Genetics, Japan
[e] Department of Biological Science, Faculty of Science, Shizuoka University, Japan

ARTICLE INFO

Keywords:
Simulation
Surface growth
Developmental process
Quantitative approach
Conformal map

ABSTRACT

The three-dimensional (3D) morphologies of many organs in organisms, such as the curved shapes of leaves and flowers, the branching structure of lungs, and the exoskeletal shape of insects, are formed through surface growth. Although differential growth, a mode of surface growth, has been qualitatively identified as 3D morphogenesis, a quantitative understanding of the mechanical contribution of differential growth is lacking. To address this, we developed a quantitative inference method to analyze the distribution of the area expansion rate, which governs the growth of surfaces into 3D morphology. To validate the accuracy of our method, we tested it on a basic 3D morphology that allowed for the theoretical derivation of the area expansion rate distribution, and then assessed the difference between the predicted outcome and the theoretical solution. We also applied this method to complex 3D shapes and evaluated its accuracy through numerical experiments. The findings of the study revealed a linear decrease in error on a log–log scale with an increase in the number of meshes in both evaluations. This affirmed the reliability of the predictions for meshes that are sufficiently refined. Moreover, we employed our methodology to analyze the developmental process of the Japanese rhinoceros beetle *Trypoxylus dichotomus*, which is characterized by differential growth regulating 3D morphogenesis. The results indicated a notably high rate of area expansion on the left and right edges of the horn primordium, which is consistent with the experimental evidence of a higher rate of cell division in these regions. Hence, these findings confirm the efficacy of the proposed method in analyzing biological systems.

1. Introduction

Surface growth contributes to the three-dimensional (3D) morphology of organs in many organisms. This includes the shape of leaves and flowers (Liang & Mahadevan, 2009, 2011; Nath et al., 2003), lung morphogenesis (Clément et al., 2012), and the shapes of diverse insect exoskeletons (Adachi et al., 2020a; Adachi et al., 2020b; Matsuda et al., 2017). One growth mode is known as differential growth, which refers to how the growth rate differs depending on the region. From a geometric perspective, differential growth is a deformation characterized by an isotropic expansion of the area at each point on a surface, with expansion rates that vary spatially. For example, the frilled and bowl-shaped forms seen in the leaves and flowers of plants are created through the growth of cell sheets. The former is formed by a higher frequency of cell proliferation at the margins of the sheet compared to the center, while the latter is formed by a higher frequency of cell proliferation at the center of the sheet compared to the margins (Liang & Mahadevan, 2009, 2011; Nath et al., 2003). The shapes of diverse insect exoskeletons are also formed by the growth of epithelial cell sheets in their primordial shapes (Adachi et al., 2020b; Matsuda et al., 2017). In the horn primordia formation of the Japanese rhinoceros beetle *Trypoxylus dichotomus*, a relationship was observed between the spatial distribution of cell division frequency during the formation of the horn primordium and the length of the branching of the post-pupal horn shape (Adachi et al., 2020a).

Despite a qualitative insight into the significance of differential

* Corresponding authors.
E-mail addresses: morikawa.kentaro.68a@kyoto-u.jp (K. Morikawa), inoue.yasuhiro.4n@kyoto-u.ac.jp (Y. Inoue).

https://doi.org/10.1016/j.jtbi.2023.111650
Received 24 March 2023; Received in revised form 17 October 2023; Accepted 20 October 2023
Available online 24 October 2023
0022-5193/© 2023 The Author(s). Published by Elsevier Ltd. This is an open access article under the CC BY license (http://creativecommons.org/licenses/by/4.0/).

京都大学 KYOTO UNIVERSITY
A Self-archived copy in
Kyoto University Research Information Repository
https://repository.kulib.kyoto-u.ac.jp
京都大学学術情報リポジトリ KURENAI 紅 Kyoto University Research Information Repository

growth in the 3D morphogenesis of various organisms, a quantitative understanding of the mechanical contribution of this growth mode to 3D morphogenesis is lacking. It is imperative to develop a quantitative approach to differential growth to determine if it is sufficient to explain the formation of 3D shapes, or if a combination of differential growth and other control mechanisms determines these shapes. Additionally, to what extent does differential growth contribute to the dynamics of shape formation in conjunction with other control mechanisms? In this study, we present an inference method for determining the spatial distribution of differential growth, specifically the area expansion rate distribution governing growth, from geometry data before and after surface growth. Our approach is validated through theoretical solutions, numerical experiments, and its application to the horn primordia formation of *Trypoxylus dichotomus*, the Japanese rhinoceros beetle. By identifying the area expansion rate distribution governing growth, we can investigate the role of differential growth in shaping 3D organ morphology across various organisms. Moreover, our approach can aid in determining the extent of differential growth's contribution to shape formation dynamics, in conjunction with other control mechanisms. Overall, the inference method developed in this study holds the potential to provide novel insights into the mechanisms driving 3D morphogenesis in a broad range of organisms.

2. Methods

This section describes a method for inferring the distribution of the area expansion rates from the pre- and post-growth shape data of a surface, along with methods for validating the inferring method.

2.1. Inference method for area expansion rate distribution

From a geometric perspective, differential growth is a deformation characterized by an isotropic expansion of the area at each point on a surface, with expansion rates that vary spatially. Thus, it corresponds to a deformation wherein the pre- and post-growth shapes are related through a conformal map, which is a map that locally preserves angles. Accordingly, the objective was to construct a conformal map between the pre- and post-growth shapes (Fig. 1a). One well-established method for constructing conformal maps for surfaces is conformal parameterization, which involves the mapping of surfaces onto a planar domain (Cartade et al., 2013; Eck et al., 1995; Lévy et al., 2002; Sheffer et al., 2005). On the other hand, in this study, we assumed that the pre- and post-growth shapes were both curved; thus, utilizing conformal parameterization alone was inadequate. We constructed a conformal map between curved surfaces via a planar domain, applying conformal parameterization. Conformal parameterization often utilizes triangular meshes as representations of surface shapes, which we align with in this study (Eck et al., 1995; Lévy et al., 2002; Sheffer et al., 2005). First, we performed conformal parameterization for the pre- and post-growth shapes, respectively. We then constructed a conformal map between the pre- and post-growth (curved) shapes through the conformal parameterizations (Fig. 1b) and computed the area expansion rate distribution using the conformal map.

2.1.1. Harmonic parameterization

Surface theory involves applying a conformal map from a surface that is homeomorphic to the disk onto the unit disk, and this conformal map is unique when the boundary is fixed (Riemann mapping theorem) (Ahlfors, 1978; Riemann, 1851). However, in the case of a polyhedron consisting of a triangular mesh (piecewise linear surface), there is no conformal map to the plane, i.e., no parameterization that preserves the interior angles of each triangle. Therefore, conformal parameterization must be an approximation, although one that corresponds to a solution as a surface theory does exist. Harmonic parameterization is one of the approximate methods for conformal parameterization that we used in this study (Eck et al., 1995).

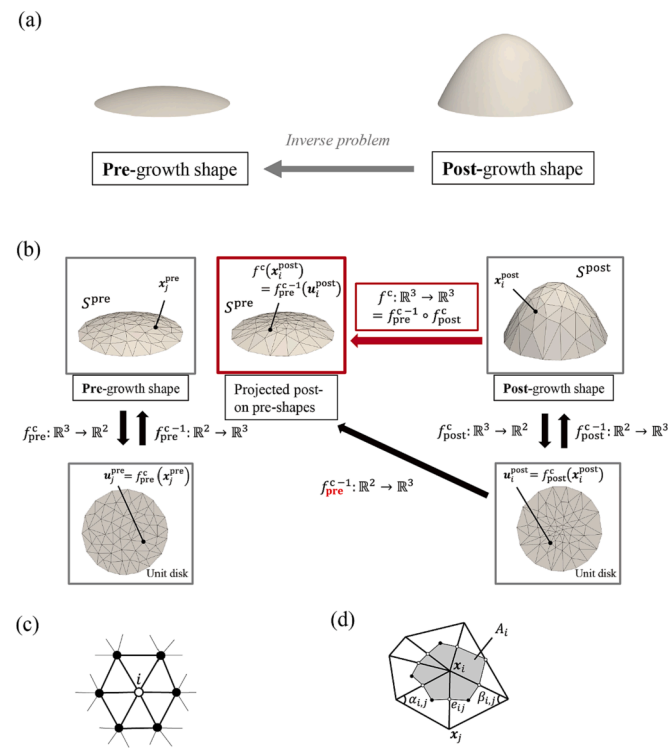

Fig. 1. Description of the method. (a) Problem description. (b) Method for constructing a conformal map from the post-growth shape to the pre-growth shape. (c) The polygon N_i consisting of the images of the vertices adjacent to i (the black dots). (d) The angles $\alpha_{i,j}$ and $\beta_{i,j}$ of the two triangles sharing the edge e_{ij} and Voronoi area A_i. The black dots indicate the centroids of triangles and the white dots indicate the midpoints of edges.

Harmonic parameterization is a method for constructing an approximate conformal map $f^{\mathrm{c}}_{\mathrm{param}}$ that maps a surface S represented by a triangular mesh onto a planar domain. The method is as follows: let V_{bnd} be the set of boundary vertices, V_{int} be the set of interior vertices of S, and $\boldsymbol{u}_i = (u_i, v_i) = f^{\mathrm{c}}_{\mathrm{param}}(\boldsymbol{x}_i)$ be the image of vertex i's position $\boldsymbol{x}_i = (x_i, y_i, z_i)$ in S. The condition for the image of vertex $i \in V_{\mathrm{int}}$ by $f^{\mathrm{c}}_{\mathrm{param}}$ to be in the polygon N_i consisting of the vertices adjacent to i (Fig. 1c) is as follows:

$$\boldsymbol{u}_i = \sum_{j \in N_i} c_{ij} \boldsymbol{u}_j, \quad \sum_{j \in N_i} c_{ij} = 1 \quad (c_{ij} > 0). \tag{1}$$

Given a triangular mesh homeomorphic to the disk, if $\boldsymbol{u}_i (i \in V_{\mathrm{bnd}})$ lies on a convex polygon and satisfies Eq. (1), then this is an injective (no self-intersection) parametrization (Tutte, 1960). The condition Eq. (1) can be rewritten as:

$$0 = \sum_j a_{ij} \boldsymbol{u}_j \tag{2}$$

with the following coefficient a_{ij}:

$$a_{ij} \begin{cases} > 0 & (\text{if } \ j \in N_i) \\ = 0 & (\text{if } \ j \notin N_i \text{ and } \ i \neq j) \\ = -\sum_{j \neq i} a_{ij} & (\text{if } \ i = j) \end{cases} \tag{3}$$

Writing this separately for interior and boundary vertices, it becomes:

$$\sum_{j \in N_{\mathrm{int}}} a_{ij} \boldsymbol{u}_j = -\sum_{j \in N_{\mathrm{bnd}}} a_{ij} \boldsymbol{u}_j. \tag{4}$$

To determine the coefficient a_{ij}, we can utilize the discrete Laplace–Beltrami operator on surface S:

京都大学 KYOTO UNIVERSITY
A Self-archived copy in
Kyoto University Research Information Repository
https://repository.kulib.kyoto-u.ac.jp
京都大学学術情報リポジトリ KURENAI 紅 Kyoto University Research Information Repository

$$a_{ij} = \begin{cases} \frac{1}{2A_i}\left(\cot\alpha_{i,j} + \cot\beta_{i,j}\right) & (\text{if } \ j \in N_i) \\ 0 & (\text{if } \ j \notin N_i \ \text{ and } \ i \neq j) \\ -\sum_{j \neq i} a_{ij} & (\text{if } \ i = j) \end{cases} \tag{5}$$

By employing the discrete Laplace–Beltrami operator as the coefficient a_{ij}, the resulting map becomes an approximate conformal map (Eck et al., 1995). Here, $\alpha_{i,j}$ and $\beta_{i,j}$ are the interior angles of the two triangles sharing the edge e_{ij} that connects the adjacent vertex j to vertex i, corresponding to the opposite angles of e_{ij} as shown in Fig. 1d. A_i is the Voronoi area for vertex i, which is computed as the sum of the fractional Voronoi areas around vertex i (Fig. 1d). The fractional Voronoi areas are calculated as follows: in the case of acute triangles, they correspond to the area of the quadrilateral composed of vertex i, midpoints of edges, and centroids; in the case of obtuse triangles, they correspond to the area of quadrilateral (when vertex i is the obtuse angle) or triangle (when a vertex other than i forms the obtuse angle) composed of vertex i and midpoints of edges.

In this study, we set the image of the boundary vertices $\boldsymbol{u}_i (i \in V_{\text{bnd}})$ on the unit circle. We obtain $\boldsymbol{u}_i (i \in V_{\text{int}})$ by solving Eq. (4) under this boundary condition.

2.1.2. Inference of the area expansion rate distribution

To construct a conformal map f^{c} that maps the post-growth shape S^{post} to the pre-growth shape S^{pre}, we first mapped each shape to the unit disk region on the plane by harmonic parameterization. We let $f^{\text{c}}_{\text{post}}$ and $f^{\text{c}}_{\text{pre}}$ be the map from S^{post} and S^{pre} to the unit disk, respectively. They map the vertex position $\boldsymbol{x}_i = (x_i, y_i, z_i)$ on S, which represents either S^{post} or S^{pre} in context, to the position $\boldsymbol{u}_i = (u_i, v_i)$ on unit disk. The image $\boldsymbol{u}$ of a point $\boldsymbol{x}$ in a triangle on the surface, but not on the vertices, is determined by the following interpolation formula:

$$\boldsymbol{u} = \frac{A_{t_1}}{A}\boldsymbol{u}_{t_1} + \frac{A_{t_2}}{A}\boldsymbol{u}_{t_2} + \frac{A_{t_3}}{A}\boldsymbol{u}_{t_3}, \quad A = A_{t_1} + A_{t_2} + A_{t_3}, \tag{6}$$

where $\boldsymbol{u}_{t_i} (i = 1, 2, 3)$ is the image of the vertex position $\boldsymbol{x}_{t_i} (i = 1, 2, 3)$ of the triangle t and $A_{t_i} (i = 1, 2, 3)$ is the area of the three triangles obtained by linking $\boldsymbol{x}$ with $\boldsymbol{x}_{t_i} (i = 1, 2, 3)$.

The mapping of the post-growth shape to the pre-growth shape is constructed as follows: first, the point $\boldsymbol{x}$ on the post-growth shape was mapped to $\boldsymbol{u}^{\text{post}}$ on the plane by $f^{\text{c}}_{\text{post}}$, and then it was mapped onto the pre-growth shape using the inverse function of $f^{\text{c}}_{\text{pre}}$. That is, the conformal map f^{c} was constructed as a composite function of $f^{\text{c}}_{\text{post}}$ and $f^{\text{c}-1}_{\text{pre}}$ (Fig. 1b):

$$f^{\text{c}} = f^{\text{c}-1}_{\text{pre}} \circ f^{\text{c}}_{\text{post}} \tag{7}$$

Since $f^{\text{c}}_{\text{post}}$ is an approximate conformal map from the surface S^{post} to the unit disk and $f^{\text{c}-1}_{\text{pre}}$ is an approximate conformal map from the unit disk to the surface S^{pre}, $f^{-1}_{\text{pre}} \circ f_{\text{post}}$ is also an approximate conformal map. Here, by using the interpolation formula Eq. (6), the inverse map $f^{\text{c}-1}_{\text{pre}}$ can be defined for any point on the unit disk. This means that the conformal map f^{c} can handle cases in which the post-growth shape and the pre-growth shape have different mesh connectivity.

Once the conformal map f^{c} from the post-growth shape S^{post} to the pre-growth shape S^{pre} was constructed as above, from the area A^{post}_t of each triangle t on S^{post} and the area of the image A^{pre}_t, the area expansion rate distribution was computed as follows:

$$R_t = \frac{A^{\text{post}}_t}{A^{\text{pre}}_t} \quad (t = 1, 2, \cdots, N_{\text{T}}), \tag{8}$$

where N_{T} is the number of triangles in the mesh.

3. Validation

To assess the validity of the inference method, a comparison is made between the predicted area expansion rate distribution and the actual distribution. For simple shape data with available theoretical solutions for conformal maps, the inference result is compared to the area expansion rate distribution derived from the theoretical solution. However, for complex shapes where theoretical solutions are not readily available, the predicted area expansion rate distribution is compared to the actual distribution through numerical experiments. These experiments involve generating shape data using the forward growth simulation method that conforms to the given area expansion rate distributions, which serve as benchmarks for the comparison.

This comparison approach enables the examination of the validity of the inference method, ensuring its accuracy for both simple and complex shapes. The evaluation metric for validity is based on the degree of agreement between the predicted and actual distributions. The forward growth simulation method employed in the numerical experiments allows the generation of shape data that conforms to the given area expansion rate distributions, providing accurate benchmarks for the comparison.

It is important to note that the accuracy of the predicted area expansion rate distribution needs to be evaluated through numerical experiments for complex shapes. In contrast, the theoretical solutions for conformal maps provide an accurate representation of the area expansion rate distribution for simple shapes. Overall, this comparison-based evaluation approach ensures the reliability of the inference method, enabling the accurate prediction of area expansion rate distributions in a wide range of shapes.

3.1. Evaluation metric for the validity of inference simulations

Let N_{T} be the number of triangles in the mesh, $R^{\text{sim}}_t (t = 1, 2, \cdots, N_{\text{T}})$ be the predicted area expansion rate distribution, and $R^{\text{true}}_t (t = 1, 2, \cdots, N_{\text{T}})$ be the true area expansion rate distribution. As the evaluation metric for the validity of the inference, we used the mean squared error (MSE) of area expansion rate distributions:

$$MSE_{\text{aer}} = \frac{1}{N_{\text{T}}} \sum_i^{N_{\text{T}}} \left(R^{\text{sim}}_i - R^{\text{true}}_i\right)^2 \tag{9}$$

3.2. Forward growth simulation

We used simulated annealing for the forward growth simulations (Kirkpatrick et al., 1983) and minimized the following energy function E:

$$E = E^{\text{Area}} + E^{\text{IA}} + E^{\text{DA}}, \tag{10}$$

$$E^{\text{Area}} = \sum\nolimits_t^{N_{\text{T}}} \frac{1}{2} k_{\text{Area}} \frac{\left(A_t - A^{\text{tgt}}_t\right)^2}{A^{\text{tgt}}_t \cdot A^{\text{tgt}}_{\text{total}}}, \quad A^{\text{tgt}}_t = R_t A^{\text{init}}_t, \quad A^{\text{tgt}}_{\text{total}} = \sum\nolimits_t^{N_{\text{T}}} A^{\text{tgt}}_t, \tag{11}$$

$$E^{\text{IA}} = \sum\nolimits_t^{N_{\text{T}}} \frac{1}{2} k_{\text{IA}} \sum\nolimits_j^3 \left(\frac{\theta^{\text{IA}}_{t,j}}{\theta^{\text{IA,tgt}}_{t,j}} - 1\right)^2 \cdot \frac{\frac{1}{2}\left(L^{\text{tgt}}_{t,j,1} + L^{\text{tgt}}_{t,j,2}\right)}{P^{\text{tgt}}_{\text{total}}}, \quad P^{\text{tgt}}_{\text{total}} = \sum\nolimits_t^{N_{\text{T}}} P^{\text{tgt}}_t, \tag{12}$$

$$E^{\text{DA}} = \sum\nolimits_e^{N_{\text{E}}} k_{\text{DA}} \frac{3\left(L^{\text{tgt}}_e\right)^2}{A^{\text{tgt}}_{e_1} + A^{\text{tgt}}_{e_2}} \left(2\tan\frac{\theta^{\text{DA}}_e}{2} - 2\tan\frac{\theta^{\text{DA,tgt}}_e}{2}\right)^2, \quad L^{\text{tgt}}_e = \sqrt{\frac{R_{e_1} + R_{e_2}}{2}} L^{\text{init}}_e, \tag{13}$$

where $E^{\text{Area}}, E^{\text{IA}}$, and E^{DA} are the energies to bring the area A_t, interior angle $\theta^{\text{IA}}_{t,j} (j = 1, 2, 3)$ of triangle t, and dihedral angle θ^{DA}_e between the triangle e_1 and e_2 that share the edge e close to their target value A^{tgt}_t,

京都大学 KYOTO UNIVERSITY
A Self-archived copy in
Kyoto University Research Information Repository
https://repository.kulib.kyoto-u.ac.jp
京都大学学術情報リポジトリ KURENAI 紅 Kyoto University Research Information Repository

$\theta_{t,j}^{\mathrm{IA,\,tgt}}$, and $\theta_e^{\mathrm{DA,\,tgt}}$, respectively (Grinspun et al., 2003; Tamstorf & Grinspun, 2013). The area expansion rate is represented by the variable R_t, and the target area of triangle t is defined as R_t times the initial area A_t^{init}. $L_{t,j,k}^{\mathrm{tgt}}$ in the definition of E^{IA} is the target length of edge k sharing the vertex j of triangle i, P_i^{tgt} is the target perimeter (sum of target edge lengths) of the triangle, $\theta_e^{\mathrm{DA,\,tgt}}$ in the definition of E^{DA} is the target dihedral angle between triangles sharing the edge e, L_e^{init} is the initial length of edge e, and N_{E} is the number of inner edges of the surface.

The procedure for simulated annealing is as follows:

1. Randomly select vertex i and move its position virtually by a small distance Δr in a random direction.

2. Calculate the energies E and E' before and after the move, and calculate the difference $\Delta E = E' - E$.

3. Accept the vertex move with the following probability according to the value of ΔE.

$$P = \min(1, \exp(-\beta \Delta E)), \tag{14}$$

where β is a parameter called inverse temperature that represents the strength of stochasticity.

4. Repeat procedures 1, 2, and 3 above with increasing β.

In this study, we performed annealing by repeating n_1 steps at β_1, followed by n_2 steps at $\beta_2 (> \beta_1)$, where one step involves performing the procedures 1, 2, and 3 once for all vertices, in a random order. Note that simulations using only the above energy function will often trap in the local energy minima, in spite of stochasticity. The reason is that once a surface with a folded shape is formed, a large energy barrier must be exceeded to eliminate the fold. To solve this problem, in addition to E^{Area}, E^{IA}, and E^{DA}, at the beginning of the simulation, the energy needed to increase the lumen volume V

$$E^{\mathrm{Vol}} = \frac{1}{2} k_{\mathrm{Vol}} \left(\frac{V}{V^{\mathrm{tgt}}} - 1 \right)^2 \tag{15}$$

is added to the energy function to prevent folding. E^{Vol} is removed after some steps, and $E = E^{\mathrm{Area}} + E^{\mathrm{IA}} + E^{\mathrm{DA}}$ is minimized. It should be noted that E^{Vol} is introduced solely to avoid being trapped in local energy minima and does not represent a biologically grounded model involving the growth process of lumen volume. The target value V^{tgt} is set sufficiently large through a trial-and-error process to prevent trapping in the local energy minima.

It should also be noted that achieving exact realization of the given area expansion rate distribution and precise conformality during the growth simulation may not always be possible. In other words, both E^{Area} and E^{IA} are expected to be non-zero, unlike the case where exact realization of both is achieved. This discrepancy would introduce additional errors that are separated from the errors associated with our inference method.

3.3. Materials and methods in the experiment

In order to confirm the efficacy of our method in analyzing biological systems, we applied it to the actual process of forming the Japanese rhinoceros beetle horn primordium. Here, we describe the materials and methods of our experiments to obtain data on the beetle horn primodium shape.

Insects. *Trypoxylus dichotomus* larvae were purchased from Loiinne (Japan). The sex of the last instar larvae was determined following previous studies (Ito et al., 2013), and the larvae were then individually fed on humus in plastic containers, and kept at 10 °C until use. Larvae were moved to room temperature for at least 10 days and reared at 28 °C. The sampling of horn primordia (24 and 48 h) followed previous studies (Morita et al., 2019).

Micro-CT analysis. Male head tissue was fixed in Carnoy solution overnight at room temperature and washed in 70 % ethanol. The sample was rehydrated through a graded ethanol series, and stained with 25 % Lugol solution (Degenhardt et al., 2010; Metscher, 2009a, 2009b) for 7 days. The stained sample was scanned using an X-ray micro-CT device (ScanXmate-E090S105, Comscantechno Co., Ltd., Japan) at a tube voltage peak of 85 kVp and a tube current of 90 μA. The sample was rotated 360 degrees in 0.24-degree increments, generating 1500 projection images of 992 × 992 pixels. The micro-CT data were reconstructed at an isotropic resolution of 13.0 μm (pre-growth stage) and 13.5 μm (post-growth stage) and converted into a 16-bit Dicom image dataset using coneCTexpress software (Comscantechno Co., Ltd., Japan). The epithelial sheet shape data were extracted by segmenting the Dicom image dataset using 3D Slicer software (Kikinis et al., 2014).

3.3.1. Evaluation method for robustness against data noise

We evaluated the robustness of our method against data noise by introducing random perturbations to the vertex positions of post-growth shape data. The magnitude of the noise was quantified using the MSE of the vertex positions:

$$MSE_{\mathrm{vtx}} = \frac{1}{N_{\mathrm{V}}} \sum_i^{N_{\mathrm{V}}} \frac{\left(\boldsymbol{x}_i^{\mathrm{noise}} - \boldsymbol{x}_i \right)^2}{A^{\mathrm{ref}}}, \tag{16}$$

where N_{V} is the total number of vertices in the mesh, $\boldsymbol{x}_i^{\mathrm{noise}}$ represents the perturbed vertex position, $\boldsymbol{x}_i$ represents the original vertex position, and A^{ref} is the total area of the reference mesh. We compared the area expansion rate distributions obtained from the perturbed data and the original data using MSE_{aer} (Eq. (9)) as a metric.

4. Validation using synthetic data

The validity of the proposed method in Section 2.1 was assessed in two steps. Firstly, the method's predicted area expansion rate distribution was compared with the theoretical solution for spherical pre- and post-growth shapes where a theoretical solution was available. Next, numerical experiments were conducted to evaluate the method's validity for several shapes that lacked theoretical solutions.

4.1. Validation through theoretical solutions

We applied this method to infer the expansion rate distribution of the growth from a spherical cap to a hemisphere, as shown in Fig. 2a-c. For this case, the theoretical solution of the conformal map could be derived (Supplementary Text 1). We used the spherical cap cut from a sphere of radius $R_2 = 2.6$ with height $h = 0.2$ as the pre-growth shape and the hemisphere of radius $R_1 = 1.0$ as the post-growth shape. The number of triangles in both the pre- and post-growth shapes was 6,000. The area expansion rate distribution R_i^{th} obtained by theoretical solution and R_i^{sim} inferred by the proposed method are shown in Fig. 2d and e, respectively. The area expansion rate distributions appeared to be almost identical. To quantitatively evaluate the discrepancy with the theoretical solution, the MSE between the area expansion rate distributions was calculated. The calculation result was 7.73×10^{-5}. This error from the theoretical solution is considered to be due to the fact that the surface is represented by a triangular mesh, and the mapping of the vertex positions is calculated by first-order interpolation (Eq. (6)). Therefore, the error from the theoretical solution changes depending on the mesh size. We conducted the same comparison for the same pre- and post-growth shapes with other numbers of triangles in a mesh. The error from the theoretical solution with respect to the number of triangles is shown in Fig. 2f. This result indicates that the order of accuracy of the inference method appeared to be $O(N_{\mathrm{T}})$. Therefore, it was confirmed that we would obtain the correct distribution by our inference method with a sufficient number of triangles in the mesh.

Our method was based on the capacity to express differential growth through a conformal map. We found that the area expansion rate dis-

京都大学 KYOTO UNIVERSITY
A Self-archived copy in
Kyoto University Research Information Repository
https://repository.kulib.kyoto-u.ac.jp
京都大学学術情報リポジトリ KURENAI 紅 Kyoto University Research Information Repository

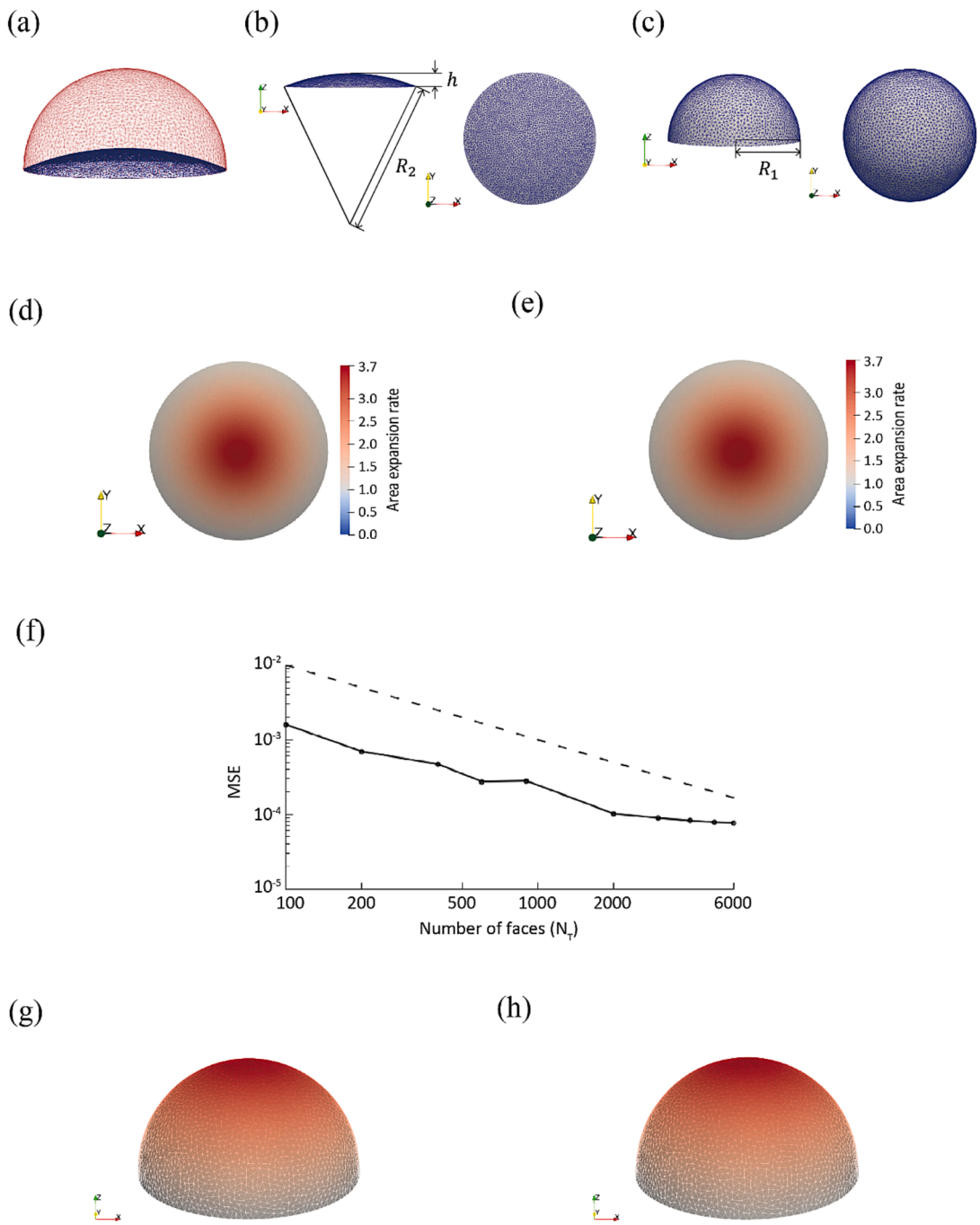

Fig. 2. Validation by the theoretical solution. (a) Problem description. The pre-growth shape shown by the blue mesh grows into the post-growth shape shown by the red mesh. (b) Pre-growth shape. Side view from the y-axis and top view from the z-axis. (c) Post-growth shape. (d) Area expansion rate distribution obtained by theoretical solution. (e) Predicted area expansion rate distribution. (f) MSE with theoretical solutions for the number of triangles in the mesh. The dashed line ($MSE \propto 10^{-N_T}$) is used as a reference slope equal to -1. (g) Forward simulation result based on the area expansion rate distribution shown in (d). (h) Forward simulation result based on the area expansion rate distribution shown in (e). (For interpretation of the references to colour in this figure legend, the reader is referred to the web version of this article.)

tribution obtained through the conformal map can effectively represent the growth from pre-growth to post-growth shapes. Thus, the forward growth simulation was performed using both the distributions obtained through the theoretical solution and the inference. The model parameters for the simulation are listed in Table 1, and the number of steps were $n_1 = 15 \times 10^4$ and $n_2 = 3 \times 10^5$. The simulation result is shown in Fig. 2g and h and Supplementary Video 1, while the energy behavior in the simulations and the computation times are shown in Supplementary Text 2. To quantitatively evaluate the discrepancy between the growth simulation results and the original post-growth shape, the MSE of vertex positions was calculated. MSE_{vtx} between the shape in Fig. 2g and the original shape was 1.64×10^{-6}, and MSE_{vtx} between the shape in Fig. 2h and the original shape was 6.20×10^{-6}. These results confirmed that the area expansion rate distribution obtained through the conformal map could govern the growth of the hemisphere.

京都大学 KYOTO UNIVERSITY
A Self-archived copy in
Kyoto University Research Information Repository
https://repository.kulib.kyoto-u.ac.jp
京都大学学術情報リポジトリ KURENAI 紅 Kyoto University Research Information Repository

Table 1
Parameters for the forward growth simulation.

Symbol	Value	Description
β_1	1.0×10^3	Inverse temperature for the first n_1 steps
β_2	1.0×10^6	Inverse temperature for the first n_2 steps
k_{Area}	1.0×10^4	Constant of area energy
k_{IA}	1.0×10^5	Constant of interior angle energy
k_{DA}	$\begin{cases} 2.0 \times 10^{-2} \\ 2.0 \times 10^{-3} \end{cases}$	Constant of dihedral angle energy for the first n_1 steps Constant of dihedral angle energy for the second n_2 steps
k_{Vol}	$\begin{cases} 9.68 \times 10^3 \\ 0.0 \end{cases}$	Constant of volume energy for the first n_1 steps Constant of volume energy for the second n_2 steps
V^{tgt}	2.2	Target value of volume
$\theta_{t,j}^{\mathrm{IA,\,tgt}}$	$\theta_{t,j}^{\mathrm{IA,\,init}}$	Target values of interior angles (set to their initial value)
$\theta_e^{\mathrm{DA,tgt}}$	0.0	Target values of dihedral angles (set to their flat state)

4.2. Validation through numerical experiments

We utilized the spherical cap as the pre-growth shape, which corresponds to the shape employed in Section 3.1. For the post-growth shape, we employed a variety of shapes shown in Fig. 3a, which were obtained through the forward growth simulations based on the area expansion rate distributions shown in Fig. 3b. The total number of triangles in all post-growth shapes was 6,000. The parameters in the forward simulations were employed with the same values as in Section 3.1 (Table 1), except for k_{Vol} and V^{tgt}. The parameters for volume energy and the steps for n_1 and n_2 are listed in Table 2. The energy behavior in the simulations and the computation times are shown in Supplementary Text 2. In these growth simulations, it was not possible to achieve exact conformal growth as desired. Consequently, the area energy E^{Area} and the interior angle energy E^{IA} retained non-zero values, even in the final state. The specific values varied depending on the shape under consideration. Fig. 3d shows the E^{Area} and E^{IA} of each shape in its final state, respectively. The results revealed that the clover-like shape (the middle of Fig. 3a) and the overhang shape (the rightmost side of Fig. 3a) exhibited significant non-zero values for both E^{Area} and E^{IA}. For the post-growth shape shown in Fig. 3a, we inferred the area expansion rate distribution using the proposed method (Fig. 3c). The results show that the predicted area expansion rate distribution appeared to be almost the same as the correct distributions given as the benchmark (Fig. 3b and c). As in Section 3.1, we also inferred the area expansion rate distribution for these shapes by varying the number of triangles and compared it with the benchmark (Fig. 3e). These results suggest that the order of accuracy of the inference method appeared to be the same as in the case of the hemisphere (Section 3.1). Therefore, we have confirmed that our inference method can obtain the correct distribution for a variety of shapes with an adequate number of triangles.

5. Applications to real data

We applied our method to the actual process of forming the Japanese rhinoceros beetle horn primordium to further confirm its validity. Furthermore, we evaluated the robustness of our method against noise using both synthetic and real data.

5.1. Application to the beetle horn primordium formation process

The horn primordium of the Japanese rhinoceros beetle is formed through the growth of an epithelial sheet inside the head capsule of the larvae (Matsuda et al., 2017). This process takes place over approximately 120 h during the prepupal stage (Morita et al., 2019). At the beginning of the prepupal stage, the epithelial sheet has a simple shape attached on the inside of the head capsule, and after approximately 48 h, it grows to form a mushroom-like shape. After approximately 120 h, fine wrinkles form on the mushroom-shaped surface, completing the horn primordium. The wrinkled mushroom shape then unfolds to form the pupal horn shape.

We applied our inference method to the analysis of the mushroom-shape formation process. The surface shapes of the epithelial sheets, including the horn primordia, were extracted from the CT data (Fig. 4a). The post-growth shape had dimensions of 8.6 mm (x), 6.5 mm (y), and 2.1 mm (z), with 6,000 triangles and an average edge length of 0.19 mm for each triangle in the mesh. The number of triangles in the pre-growth mesh was 3,000. These are the regions of the epithelial sheets inside the head capsules that are as extensive as feasible, including the horn primordia. After applying our method to these areas, we also examined the regions that were considered most likely to be involved in the formation of the horn primordium.

The inference result of applying our inference method to the shapes shown in Fig. 4a suggests that the predicted area expansion rate distribution is characterized by a locally concentrated expansion region (circular region in Fig. 4b), with particularly large expansion rates at the left and right edges within that expansion region (arrowhead in Fig. 4b). We also performed a forward growth simulation based on this area expansion rate distribution with $n_1 = 9 \times 10^5$ and $n_2 = 9 \times 10^5$ steps, using the parameters listed in Table 1, and parameters for volume energy were set as $k_{\mathrm{Vol}} = 9.68 \times 10^3$ and $V^{\mathrm{tgt}} = 1.0 \times 10^2$ for the first n_1 steps. The energy behavior in the simulations and the computation times are shown in Supplementary Text 2. The results show that the obtained shape is close to the shape of the real data (Fig. 4a and c). This confirms that the predicted area expansion rate distribution possibly accounts for the mushroom-shape formation of the horn primordium.

Notably, this method requires that the domains used as pre-growth and post-growth shapes are equivalent. In other words, the area expansion rate distribution is computed on the premise that the entire post-growth shape is formed by the area expansion of the entire pre-growth shape. However, as these data were extracted from CT data and encompass as extensive a domain as feasible, the pre- and post-growth domains shown in Fig. 4a may not be selected to correspond with one another. Observations suggest that in the formation of beetle horn primordia, the domains involved in formation appear to be primarily concentrated in the frons region (Fig. 4d), particularly corresponding to the lower part (Morita et al., 2019; Ohde et al., 2018). Nevertheless, it is uncertain which domains specifically correspond to the horn primordia. Thus, we also performed simulations assuming various correspondence of the domains (Fig. 4d). The results indicated that the shape of the expansion region could range from circular to elliptical, depending on how the corresponding domain was selected. In all cases, the regions with particularly high expansion rates were located at the left and right edges of the region (Fig. 4e).

Furthermore, to assess the adequacy of the mesh resolution, we made inferences of the area expansion rate distribution for the cases where the number of triangles was reduced, comparing them to the case with 6,000 triangles using the MSE. The results showed that when the number of triangles fell below 2,000, differences of approximately 10^{-1} or higher were observed, whereas when the number exceeded 2,000, the differences decreased to approximately 10^{-2} or lower (Fig. 5). Therefore, it is considered that with $N_T = 6,000$, the results have sufficiently converged.

5.2. Robustness evaluation

We performed a robustness evaluation on both the synthetic data (Fig. 2c, 3a) and the real data (Fig. 4a), assessing the impact of vertex position perturbations on the accuracy of the estimated area expansion rate distributions. Each of these meshes consists of 6,000 triangles, and the evaluation results are shown in Fig. 6. This result revealed that the MSE of the area expansion rate distribution (MSE_{aer}) increased linearly on a logarithmic scale as the MSE of vertex positions (MSE_{vtx}) increased (Fig. 6a). Fig. 6b presents the inference results for the most significant shape noise in each shape, and despite the large errors, the predicted

京都大学 KYOTO UNIVERSITY
A Self-archived copy in
Kyoto University Research Information Repository
https://repository.kulib.kyoto-u.ac.jp
京都大学学術情報リポジトリ KURENAI 紅 Kyoto University Research Information Repository

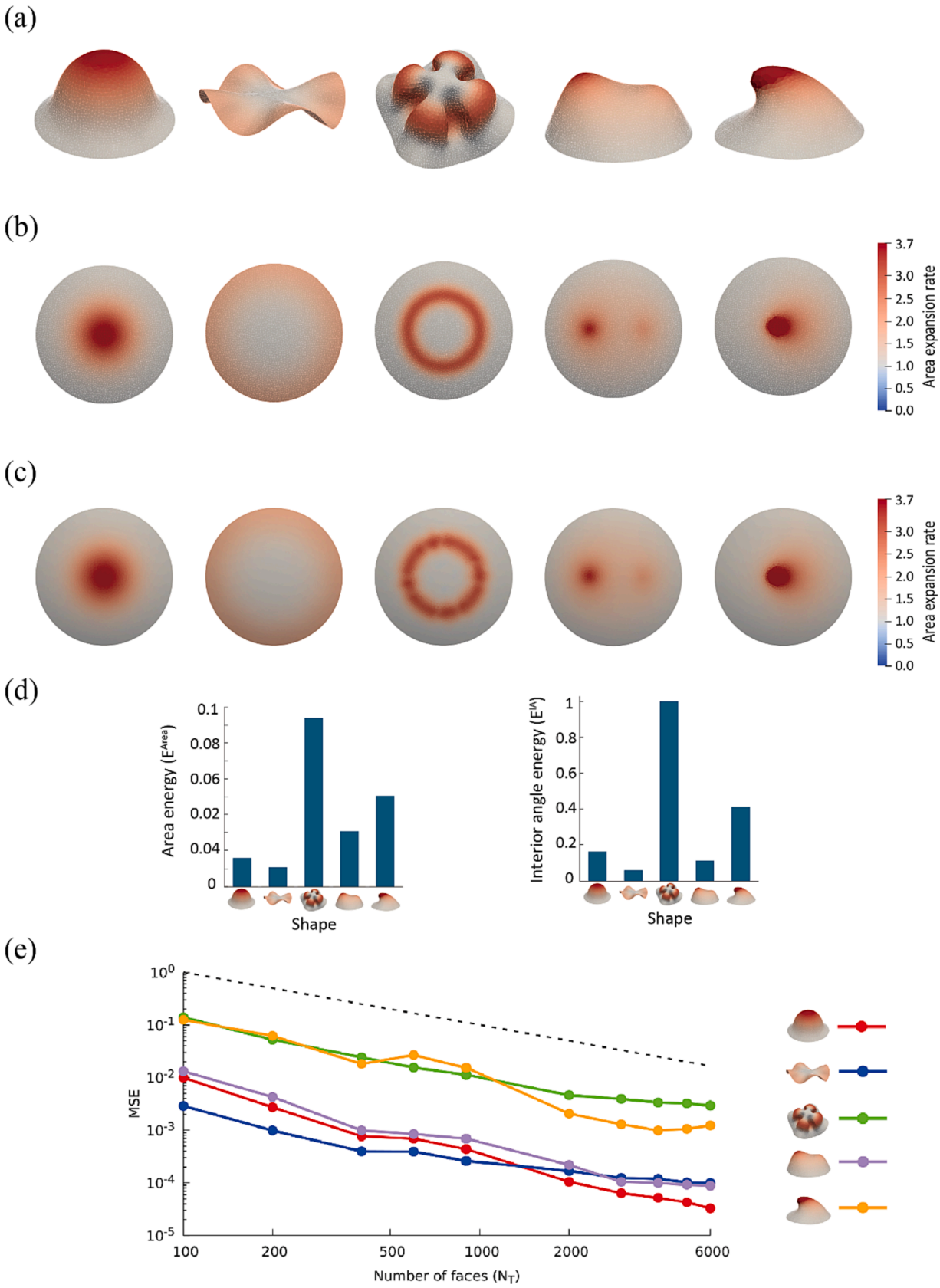

Fig. 3. Validation by numerical experiments. (a) Post-growth shape data obtained through forward-growth simulations. (b) The given area expansion rate distributions. (c) Predicted area expansion rate distributions. (d) E^{Area} and E^{IA} of each shape in its final state. (e) MSE between the given area expansion rate distributions and the predicted area expansion distributions. The dashed line ($MSE \propto 10^{-N_T}$) is used as a reference slope equal to -1.

京都大学 KYOTO UNIVERSITY
A Self-archived copy in
Kyoto University Research Information Repository
https://repository.kulib.kyoto-u.ac.jp
京都大学学術情報リポジトリ KURENAI 紅 Kyoto University Research Information Repository

Table 2
Parameters for volume energy and number of steps in the forward-growth simulations.

Symbol	Given area expansion rate distribution					Description
k_{Vol}	$\begin{cases} 4.5 \\ 0.0 \end{cases}$	$\begin{cases} 0.0 \\ 0.0 \end{cases}$	$\begin{cases} 0.0 \\ 0.0 \end{cases}$	$\begin{cases} 3.92 \\ 0.0 \end{cases}$	$\begin{cases} 3.125 \\ 0.0 \end{cases}$	Constant of volume energy for the first n_1 steps (10^3) Constant of volume energy for the second n_2 steps
V^{tgt}	2.2	–	–	1.4	1.25	Target value of volume
n_1	3	9	9	3	3	Number of the first steps for annealing (10^5)
n_2	9	9	18	9	15	Number of the second steps for annealing (10^5)

area expansion rate distributions retained the qualitative shape of the original distributions.

6. Discussion

In this study, we developed a method to infer the area expansion rate distribution by constructing a conformal map between pre- and post-growth surface shapes. Although our method uses an approximate conformal map twice, the evaluations examined in Sections 3.1 and 3.2 confirm that the inferred results converge toward the correct solution when the number of triangles in the mesh increases.

In the numerical experiments explored in Section 3.2, some of the results exhibited relatively high MSE, particularly the clover-like shape (the middle of Fig. 3a) and the overhang shape (the rightmost side of Fig. 3a). There are two possible reasons for this. First, it could be attributed to the fact that the post-growth shapes employed in the tests were created by forward simulations. In these forward simulations, minimum energy states are sought through thermal fluctuation, imposing energy that preserves the inner angles of the triangle to ensure conformality. As such, it cannot be an exact conformal growth, as shown in Fig. 3d. Second, there is no exact conformal growth corresponding to the area expansion rate distribution given as a benchmark for triangle meshes. The degree of deviation from the exact conformal map depends on the area expansion rate distribution itself. In the forward simulation, if the area expansion strictly follows the given distribution, the discrepancy of conformality increases, whereas if the conformality is strictly maintained, the discrepancy of the area expansion rate increases. Therefore, it is not possible to minimize these residuals simultaneously. This constitutes a limitation of the forward simulation conducted to verify the accuracy of the inference and is not an issue for the inference method proposed in this study.

As demonstrated in Section 4.1, our method can be applied to real data. One biological interpretation of the area expansion rate distribution is the distribution of cell proliferation frequency. Experimentally, it has been observed that cell proliferation frequency is non-uniformly distributed during the beetle horn primordium formation process (Adachi et al., 2020a). This observation suggests that, at a certain point in the mushroom-shaped formation process of the horn primordium, cell proliferation is particularly high at the left and right edges of the cell proliferation region, not the center. This distribution is correlated with the length of the branching of the pupal horn shape. This finding is consistent with the inference results from Section 4.1, indicating that regions with particularly high area expansion rates are present at the left and right edges of the expansion region. Additionally, the results indicate that the spatial distribution of cell division frequency may control the length of branching as well as the overall mushroom-shaped formation. It is important to note that our approach does not distinguish between surface deformations caused by mass-increasing growth, such as cell proliferation, and surface deformations caused by elastic stretching due to changes in lumen volume or other physical constraints. As a result, what we refer to as growth in this study may include the possibility of elastic deformation. To determine whether the mapping between the pre- and post-growth shapes includes elastic deformations, further mechanical analysis is required, considering not only the effects of area growth, but also reasonable settings for lumen volume change, physical constraints by the surrounding head capsule, and so on. Such analytical methods include forward simulations that take into account surface and bulk growth based on nonlinear elasticity in continua (Goriely, 2017; Taber, 2020). As an initial step in such examinations, the insights obtained by our method are valuable, providing a foundation for a more comprehensive analysis in future research.

As noted in Section 4.1, our method relies on the assumption that the domains of pre- and post-growth shapes are consistent. However, our method did not directly identify the correspondence between the pre- and post-growth domains. Nevertheless, the correspondence of the domains can still be investigated through a process of trial and error, with the help of experimental insights. For instance, by testing potential combinations of pre- and post-growth shapes, common features may emerge across these combinations, as shown in this study. These common features form the basis for working hypotheses for future experiments.

In this study, the quantitative validity of our inference method was verified for artificial shape data with quantitatively correct distributions. However, for real data, the verification was qualitative and did not extend to a quantitative experimental verification, as described above. To conduct such a quantitative validation, it would be necessary to track the process of area expansion through time-lapse imaging, which would enable us to obtain the correct distribution of area expansion rates. However, time-lapse imaging presents substantial experimental challenges, especially for tracking complex morphological changes during late-stage development of non-model organisms, such as beetle horns. Feasible time-lapse imaging could extend our method to encompass the correspondence within the domains of pre- and post-growth shapes. This aspect remains an intriguing research topic and a future challenge.

The accuracy of our inference method depends on the number of triangles in the mesh. In practical applications using real data, the number of triangles depends on the measuring device. In this study, a triangular mesh with an average edge length of approximately 0.19 mm allowed for accurate triangulation in regions of about 8 mm in scale, as demonstrated in Section 4.1. In many experimental setups, a similar level of precision in triangulation can be achieved.

In our robustness evaluation presented in Section 4.2, we observed a first-order power-law dependence of the difference in MSE of the area expansion rate distribution on the magnitude of shape noise. Therefore, as the magnitude of shape noise increases, inference accuracy decreases accordingly. However, it is important to note that, even in the presence of noise, the qualitative inference of the area expansion rate distribution remains consistent. Specifically, the ring-like area expansion rate distribution could be obtained even in the presence of noise for the clover-like shape in the middle of Fig. 3a. This ability to infer non-intuitive features demonstrates the effectiveness of our proposed method.

For the sake of mathematical tractability, our method assumes locally isotropic growth (conformality) as an initial approximation of morphological change through area expansion. Therefore, it cannot be applied in cases where anisotropic mechanisms, such as anisotropic elongation resulting from the orientation of the cell division axis or cell

京都大学 KYOTO UNIVERSITY
A Self-archived copy in
Kyoto University Research Information Repository
https://repository.kulib.kyoto-u.ac.jp
京都大学学術情報リポジトリ KURENAI 紅 Kyoto University Research Information Repository

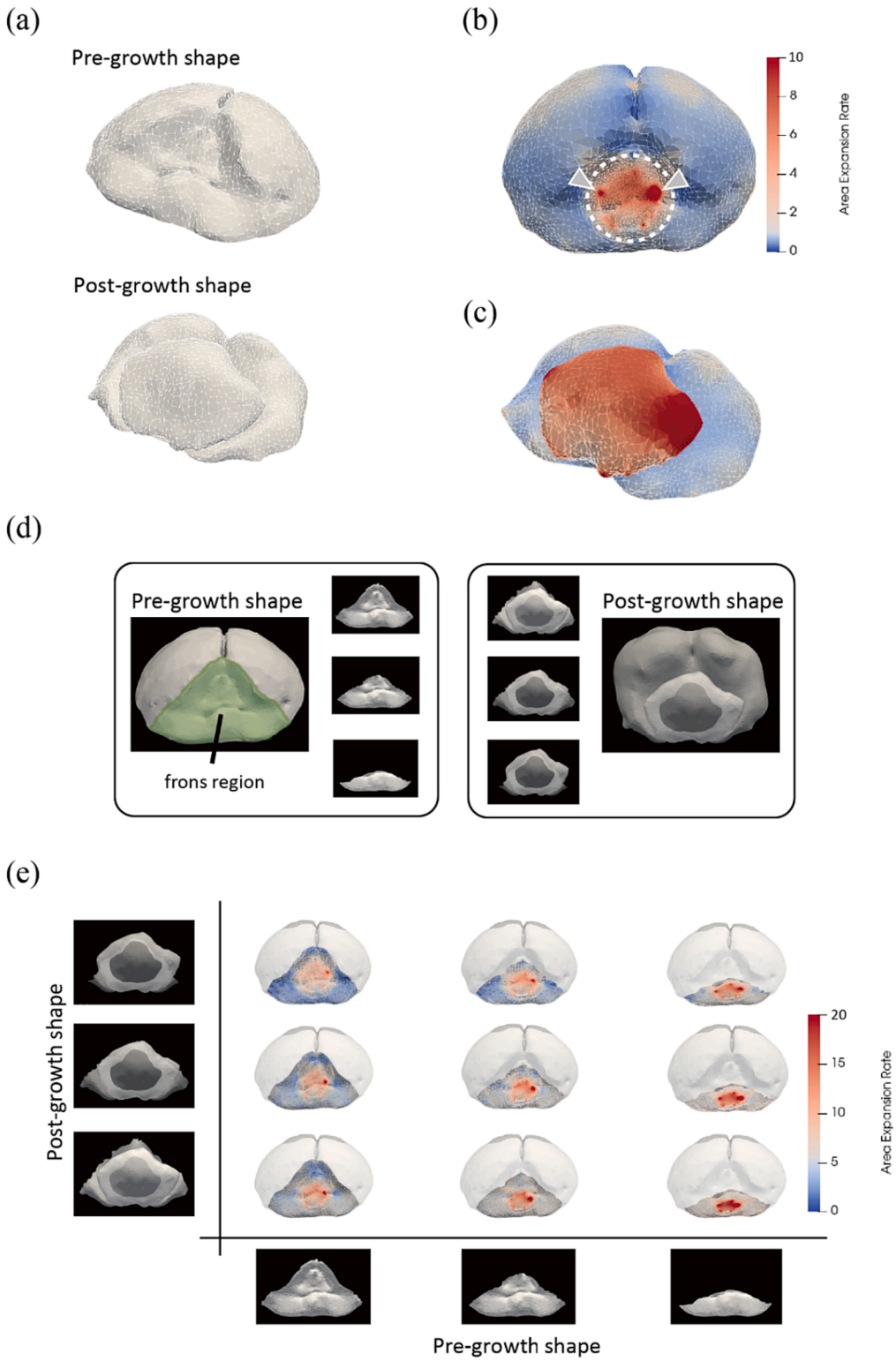

Fig. 4. Application of the beetle to the horn primordium morphogenesis, Trypoxylus dichotomus. (a) The pre- and post-growth shape CT data. (b) Predicted area expansion rate distribution of beetle horn primordium morphogenesis. There is a locally concentrated area expansion region (dotted circle), and in the expansion region, the expansion rate on the left and right sides (arrowhead) is particularly large. (c) Forward growth simulation results. The colors correspond to the colors in (b). (d) Taking the domains of the pre- and post-growth shapes into account, the region corresponding to horn primordium is considered to be limited to the frons region (Morita et al., 2019; Ohde et al., 2018). (e) Predicted area expansion rate distribution of beetle horn primordium morphogenesis for various domain configurations.

京都大学 KYOTO UNIVERSITY
A Self-archived copy in
Kyoto University Research Information Repository
https://repository.kulib.kyoto-u.ac.jp
京都大学学術情報リポジトリ KURENAI 紅 Kyoto University Research Information Repository

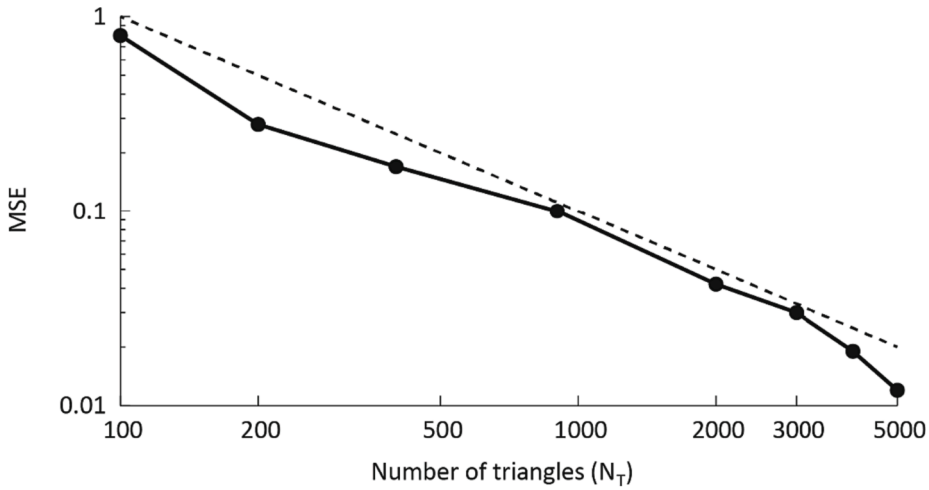

Fig. 5. The MSE between the predicted area expansion rate distributions for the case with 6,000 triangles and for the cases where the number of triangles was reduced. The dashed line ($MSE \propto 10^{-N_T}$) is used as a reference slope equal to −1.

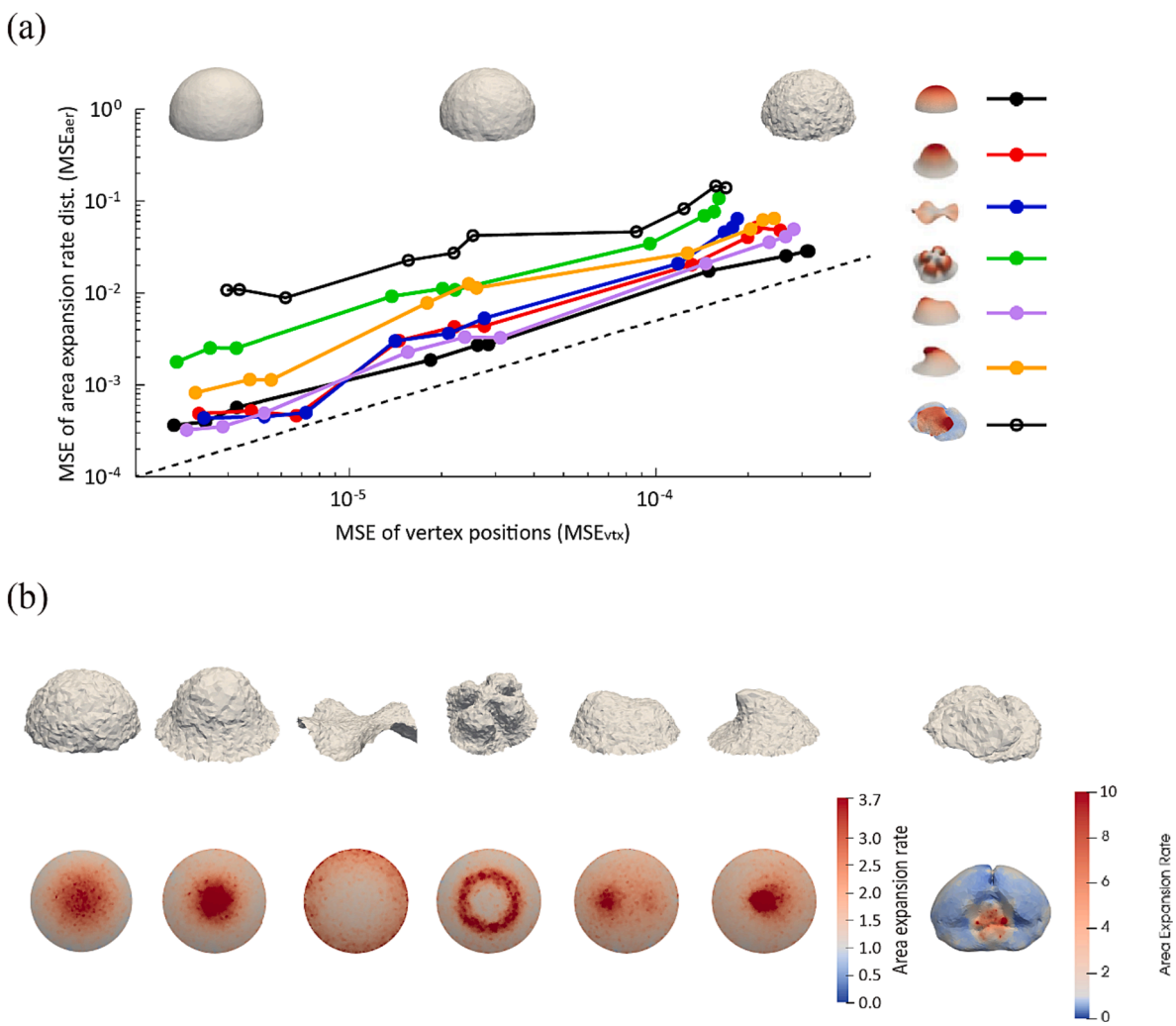

Fig. 6. (a) The relationship between the MSE of vertex positions and the MSE of area expansion rate distribution. The noisy hemisphere shapes above the graph are the shapes with corresponding MSE_{vtx} values of 2.66×10^{-6}, 2.62×10^{-5}, and 3.15×10^{-4} from left to right. The dashed line ($MSE_{\mathrm{aer}} \propto 10^{MSE_{\mathrm{vtx}}}$) is used as a reference slope equal to 1. (b) The post-growth shapes and the predicted area expansion rate distributions for the most shape-noisy cases. Noise-free cases are shown in Fig. 2e, 3c and 4b for the predicted area expansion rate distributions.

京都大学 KYOTO UNIVERSITY
A Self-archived copy in
Kyoto University Research Information Repository
https://repository.kulib.kyoto-u.ac.jp
京都大学学術情報リポジトリ KURENAI 紅 Kyoto University Research Information Repository

rearrangement, play a role (Keller et al., 1992; Mao et al., 2011; Morishita et al., 2017; Shindo et al., 2019; Tada & Heisenberg, 2012). Nonetheless, it can serve as a null hypothesis to initiate research in such cases. In traditional biological studies that employ physical simulations, simulations are feasible only after a working hypothesis is derived from significant experimental observations, and the hypothesis is subsequently tested theoretically (Inoue et al., 2016; Okamoto et al., 2013; Shindo et al., 2019; Shinoda et al., 2018). Our method in this study enables the acquisition of information on area expansion rate distribution, which is essential for forward simulations, even when significant experimental observations have not yet been conducted. This allows us to examine whether morphogenesis is governed solely by the differential growth mechanism explained by the area expansion rate distribution or if other underlying mechanisms, such as cellular activities (e.g., apical contraction, orientation of cell division, and cell migration), boundary conditions (e.g., lumen pressure), and constraints from surrounding tissues, are at play. This examination can be conducted before establishing an experimental system (Inoue et al., 2016; Keller et al., 1992; Mao et al., 2011; Milner et al., 1984; Shindo et al., 2019; Tada & Heisenberg, 2012). Moreover, our method holds the potential to be extended for inferring growth modes, including anisotropy. While such an extension might face challenges—since solutions may no longer be unique with anisotropy—experimental insights into the nature of anisotropic growth could guide an improvement of the method to obtain appropriate solutions.

Declaration of Competing Interest

The authors declare that they have no known competing financial interests or personal relationships that could have appeared to influence the work reported in this paper.

Acknowledgements

We would like to acknowledge the helpful discussions from the perspective of continuum mechanics with Dr. Hironori Takeda. We would like to thank Editage (www.editage.com) for English language editing.

Funding

This work was supported by MEXT KAKENHI (Grant Nos. 20H05947 and 20H05944), JSPS KAKENHI (Grant No. 21K15135), NIG-JOINT (42A2019 and 35A2020), and JST SPRING (Grant No. JPMJSP2110).

Appendix A. Supplementary data

Supplementary data to this article can be found online at https://doi.org/10.1016/j.jtbi.2023.111650.

References

Adachi, H., Matsuda, K., Niimi, T., Kondo, S., Gotoh, H., 2020a. Genetical control of 2D pattern and depth of the primordial furrow that prefigures 3D shape of the rhinoceros beetle horn. Sci. Rep. 10 (1), 18687. https://doi.org/10.1038/s41598-020-75709-y.

Adachi, H., Matsuda, K., Nishida, K., Hanson, P., Kondo, S., Gotoh, H., 2020b. Structure and development of the complex helmet of treehoppers (Insecta: Hemiptera: Membracidae). Zool. Lett. 6 (1), 3. https://doi.org/10.1186/s40851-020-00155-7.

Ahlfors, L.V., 1978. Complex analysis, 3rd ed. McGraw-Hill.

Cartade, C., Mercat, C., Malgouyres, R., Samir, C., 2013. Mesh parameterization with generalized discrete conformal maps. J. Math. Imaging Vision 46 (1), 1–11. https://doi.org/10.1007/s10851-012-0362-y.

Clément, R., Blanc, P., Mauroy, B., Sapin, V., Douady, S., 2012. Shape self-regulation in early lung morphogenesis. PLoS One 7 (5), e36925.

Degenhardt, K., Wright, A.C., Horng, D., Padmanabhan, A., Epstein, J.A., 2010. Rapid 3D phenotyping of cardiovascular development in mouse embryos by micro-CT with iodine staining. *Circulation*. Cardiovasc. Imag. 3 (3), 314–322. https://doi.org/10.1161/CIRCIMAGING.109.918482.

Eck, M., DeRose, T., Duchamp, T., Hoppe, H., Lounsbery, M., & Stuetzle, W., 1995. Multiresolution analysis of arbitrary meshes. Proceedings of the 22nd Annual Conference on Computer Graphics and Interactive Techniques - SIGGRAPH, *'95*, 173–182. https://doi.org/10.1145/218380.218440.

Goriely, A., 2017. The Mathematics and Mechanics of Biological Growth. Springer. https://doi.org/10.1007/978-0-387-87710-5.

Grinspun, E., Hirani, A. N., Desbrun, M., & Schröder, P., 2003. Discrete shells. In Proceedings of the 2003 ACM SIGGRAPH/Eurographics Symposium on Computer Animation, SCA 2003, pp. 62–67.

Inoue, Y., Suzuki, M., Watanabe, T., Yasue, N., Tateo, I., Adachi, T., Ueno, N., 2016. Mechanical roles of apical constriction, cell elongation, and cell migration during neural tube formation in Xenopus. Biomech. Model. Mechanobiol. 15 (6), 1733–1746. https://doi.org/10.1007/s10237-016-0794-1.

Ito, Y., Harigai, A., Nakata, M., Hosoya, T., Araya, K., Oba, Y., Ito, A., Ohde, T., Yaginuma, T., Niimi, T., 2013. The role of doublesex in the evolution of exaggerated horns in the Japanese rhinoceros beetle. EMBO Rep. 14 (6), 561–567. https://doi.org/10.1038/embor.2013.50.

Keller, R., Shih, J., Sater, A., 1992. The cellular basis of the convergence and extension of the Xenopus neural plate. Dev. Dyn. 193 (3), 199–217. https://doi.org/10.1002/aja.1001930302.

Kikinis, R., Pieper, S.D., Vosburgh, K.G., 2014. 3D Slicer: A Platform for Subject-Specific Image Analysis, Visualization, and Clinical Support. In: Jolesz, F.A. (Ed.), Intraoperative Imaging and Image-Guided Therapy. Springer, New York, pp. 277–289. https://doi.org/10.1007/978-1-4614-7657-3_19.

Kirkpatrick, S., Gelatt, C.D., Vecchi, M.P., 1983. Optimization by Simulated Annealing. Science 220 (4598), 671–680. https://doi.org/10.1126/science.220.4598.671.

Lévy, B., Petitjean, S., Ray, N., Maillot, J., 2002. Least squares conformal maps for automatic texture atlas generation. ACM Trans. Graph. 21 (3), 362–371. https://doi.org/10.1145/566654.566590.

Liang, H., & Mahadevan, L., 2009. The shape of a long leaf. *Proceedings of the National Academy of Sciences of the United States of America*, *106*(52), 22049–22054. https://doi.org/10.1073/pnas.0911954106.

Liang, H., Mahadevan, L., 2011. Growth, geometry, and mechanics of a blooming lily. PNAS 108 (14), 5516–5521. https://doi.org/10.1073/pnas.1007808108.

Mao, Y., Tournier, A.L., Bates, P.A., Gale, J.E., Tapon, N., Thompson, B.J., 2011. Planar polarization of the atypical myosin Dachs orients cell divisions in *Drosophila*. Genes Dev. 25 (2), 131–136. https://doi.org/10.1101/gad.610511.

Matsuda, K., Gotoh, H., Tajika, Y., Sushida, T., Aonuma, H., Niimi, T., Akiyama, M., Inoue, Y., Kondo, S., 2017. Complex furrows in a 2D epithelial sheet code the 3D structure of a beetle horn. Sci. Rep. 7 (1), 13939. https://doi.org/10.1038/s41598-017-14170-w.

Metscher, B.D., 2009a. Micro CT for comparative morphology: Simple staining methods allow high-contrast 3D imaging of diverse non-mineralized animal tissues. BMC Physiol. 9 (1), 11. https://doi.org/10.1186/1472-6793-9-11.

Metscher, B.D., 2009b. MicroCT for developmental biology: A versatile tool for high-contrast 3D imaging at histological resolutions. Dev. Dyn. 238 (3), 632–640. https://doi.org/10.1002/dvdy.21857.

Milner, M.J., Bleasby, A.J., Kelly, S.L., 1984. The role of the peripodial membrane of leg and wing imaginal discs of Drosophila melanogaster during evagination and differentiation in vitro. Wilhelm Roux's Arch. Dev. Biol. 193 (3), 180–186. https://doi.org/10.1007/BF00848893.

Morishita, Y., Hironaka, K.I., Lee, S.W., Jin, T., Ohtsuka, D., 2017. Reconstructing 3D deformation dynamics for curved epithelial sheet morphogenesis from positional data of sparsely labeled cells. Nat. Commun. 8 (1), 15. https://doi.org/10.1038/s41467-017-00023-7.

Morita, S., Ando, T., Maeno, A., Mizutani, T., Mase, M., Shigenobu, S., Niimi, T., 2019. Precise staging of beetle horn formation in Trypoxylus dichotomus reveals the pleiotropic roles of doublesex depending on the spatiotemporal developmental contexts. PLoS Genet. 15 (4), e1008063.

Nath, U., Crawford, B.C.W., Carpenter, R., Coen, E., 2003. Genetic Control of Surface Curvature. Science 299 (5611), 1404–1407. https://doi.org/10.1126/science.1079354.

Ohde, T., Morita, S., Shigenobu, S., Morita, J., Mizutani, T., Gotoh, H., Zinna, R.A., Nakata, M., Ito, Y., Wada, K., Kitano, Y., Yuzaki, K., Toga, K., Mase, M., Kadota, K., Rushe, J., Lavine, L.C., Emlen, D.J., Niimi, T., 2018. Rhinoceros beetle horn development reveals deep parallels with dung beetles. PLoS Genet. 14 (10), e1007651.

Okamoto, M., Namba, T., Shinoda, T., Kondo, T., Watanabe, T., Inoue, Y., Takeuchi, K., Enomoto, Y., Ota, K., Oda, K., Wada, Y., Sagou, K., Saito, K., Sakakibara, A., Kawaguchi, A., Nakajima, K., Adachi, T., Fujimori, T., Ueda, M., Hayashi, S., Kaibuchi, K., Miyata, T., 2013. TAG-1-assisted progenitor elongation streamlines nuclear migration to optimize subapical crowding. Nat. Neurosci. 16 (11), 1556–1566. https://doi.org/10.1038/nn.3525.

Riemann, B., 1851. Grundlagen für eine allgemeine Theorie der Functionen einer veränderlichen complexen. *Grosse*, Dissertation. Göttingen.

Sheffer, A., Lévy, B., Mogilnitsky, M., Bogomyakov, A., 2005. ABF++: fast and robust angle based flattening. ACM Trans. Graph. 24 (2), 311–330. https://doi.org/10.1145/1061347.1061354.

Shindo, A., Inoue, Y., Kinoshita, M., Wallingford, J.B., 2019. PCP-dependent transcellular regulation of actomyosin oscillation facilitates convergent extension of vertebrate tissue. Dev. Biol. 446 (2), 159–167. https://doi.org/10.1016/j.ydbio.2018.12.017.

Shinoda, T., Nagasaka, A., Inoue, Y., Higuchi, R., Minami, Y., Kato, K., Suzuki, M., Kondo, T., Kawaue, T., Saito, K., Ueno, N., Fukazawa, Y., Nagayama, M., Miura, T., Adachi, T., Miyata, T., 2018. Elasticity-based boosting of neuroepithelial nucleokinesis via indirect energy transfer from mother to daughter. PLoS Biol. 16 (4), e2004426.

京都大学 KYOTO UNIVERSITY
A Self-archived copy in
Kyoto University Research Information Repository
https://repository.kulib.kyoto-u.ac.jp
京都大学学術情報リポジトリ KURENAI 紅 Kyoto University Research Information Repository

Taber, L.A., 2020. Continuum Modeling in Mechanobiology. Springer. https://doi.org/10.1007/978-3-030-43209-6.

Tada, M., Heisenberg, C.P., 2012. Convergent extension: Using collective cell migration and cell intercalation to shape embryos. Development (cambridge) 139 (21), 3897–3904. https://doi.org/10.1242/dev.073007.

Tamstorf, R., Grinspun, E., 2013. Discrete bending forces and their Jacobians. Graph. Model. 75 (6), 362–370. https://doi.org/10.1016/j.gmod.2013.07.001.

Tutte, W.T., 1960. Convex Representations of Graphs. Proc. Lond. Math. Soc. s3–10(1), 304–320. https://doi.org/10.1112/plms/s3-10.1.304.